THE JOURNAL OF PHYSICAL CHEMISTRY C

Article

pubs.acs.org/JPCC

Amorphous Iron Oxyhydroxide Nanosheets: Synthesis, Li Storage, and Conversion Reaction Kinetics

Chen Xu,[†,§] Yi Zeng,[†] Xianhong Rui,[†] Jixin Zhu,[†,§] Huiteng Tan,[†,§] Antonio Guerrero,[‡] Juan Toribio,[‡] Juan Bisquert,[‡] Germà Garcia-Belmonte,*[,‡] and Qingyu Yan*[,†,§]

[†]School of Materials Science and Engineering, Nanyang Technological University, Singapore 639798, Singapore

[‡]Photovoltaic and Optoelectronic Devices Group, Departament de Física, Universitat Jaume I, 12071 Castelló, Spain

[§]TUM CREATE Research Centre@NTU, Nanyang Technological University, Singapore 637459, Singapore

Supporting Information

ABSTRACT: We present a facile approach to synthesize amorphous iron oxyhydroxide nanosheet from the surfactant-assisted oxidation of iron sulfide nanosheet. The amorphous iron oxyhydroxide nanosheet is porous and has a high surface area of 223 m^2 g^{-1}. The lithium storage properties of the amorphous iron oxyhydroxide are characterized: it is a conversion-reaction electrode material, and it demonstrates superior rate capabilities (e.g., discharge capacities as high as 642 mAh g^{-1} are delivered at a current density of 2 C). The impedance spectroscopy analysis identifies a *RC* series subcircuit originated by the conversion-reaction process. Investigation of the conversion-reaction kinetics through the *RC* subcircuit time constant reproduces the hysteresis in the discharge/charge voltage profile. Hysteresis is then connected to underlying thermodynamics of the conversion reaction rather than to a kinetic limitation.

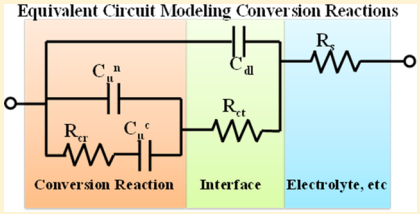

INTRODUCTION

Lithium ion battery (LIBs) are one of the most practical and promising energy storage devices.[1] Electrode materials with higher capacities, better rate capabilities, and durable cycling performance are desired for future LIBs.[1] Recently, nanostructuring has proven to be effective in improving electrochemical performance of LIBs,[2] for nanomaterials lead to increased electrode/electrolyte contact areas and shortened charge diffusion path, permitting batteries to operate at a higher power density.

Besides nanostructuring, other approaches, such as forming loosely porous network[3] and composite formation with a buffering media (e.g., graphene),[3] are effective in enhancing stress tolerance and in turn improving cycling stability. It was demonstrated that amorphous TiO_2 nanotubes possess higher capacities and better capacity retention than that of anatase-phased crystalline TiO_2 with identical morphology.[4] Amorphous hierarchical porous GeO_x was reported as a high-capacity anode with excellent cyclability in both half cells and full cells.[5] Different lithium storage properties of amorphous MoO_2 were reported as compared to its crystalline counterpart, and lithium storage at structural defects in amorphous MoO_2 was proposed.[6]

Fe_2O_3, Fe_3O_4, and FeOOH have attracted great interest in various applications due to their natural abundance and eco-friendliness.[7] Controlled synthesis of Fe_2O_3 and Fe_3O_4 nanostructures and their applications in LIBs have been intensively investigated.[8] Although the theoretical specific capacity of FeOOH is as high as 903 mAh g^{-1}, there are few reports on FeOOH as LIB anode material. Moreover, kinetics of the charge transfer process in this electrode material is not fully clear and is worth studying in detail.

Herein, we report a controlled synthetic approach to prepare amorphous FeOOH nanostructure and explore its electrochemical property as an LIB anode. The as-synthesized amorphous iron oxyhydroxide nanosheets are highly porous with a BET surface area of 223 m^2 g^{-1}. When tested as an anode in LIBs, the amorphous iron oxyhydroxide based electrode demonstrates excellent rate capabilities. Electrochemical impedance measurements are carried out to further examine the rate-limiting kinetic processes of the amorphous electrode materials. We have proposed a new equivalent circuit model that captures the discharging/charging capacitance and resistive mechanisms governed by the conversion reaction process. Moreover, a connection has been found between the characteristic frequency of the conversion reaction and the inherent hysteresis observed between charge and discharge voltage profiles.

EXPERIMENTAL SECTION

Chemical Synthesis. The amorphous iron oxide of porous nanosheets structure was synthesized by oxidation of ultrathin iron sulfide (FeS) nanosheets by H_2O_2/H_2O solution at room temperature. Synthesis of ultrathin iron sulfide has been reported previously.[9] In a typical synthesis, 44 mg of as-synthesized FeS powder is uniformly dispersed in 20 mL of toluene. 1 mmol of CTAB is dissolved into 20 mL to prepare

Received: June 13, 2013

   dx.doi.org/10.1021/jp405848j | J. Phys. Chem. C XXXX, XXX, XXX−XXX

50 mM CTAB/H_2O solution, which is then added to the FeS/toluene solution. The mixed solution is vigorously stirred and slightly heated at 40 °C until toluene is completely evaporated. After that, the solution is repeatedly washed by water until there is no bubbling upon stirring, indicating complete removal of CTAB. Then, 2 mmol of H_2O_2 is added, and stirring is continued at room temperature for 12 h. During the oxidation, the black solution gradually turns orange. The products were then washed with ethanol, followed by drying at 150 °C for 24 h.

Characterization. Morphologies were characterized by a field emission scanning electron microscope (FESEM, JEOL JSM-7600F). The HRTEM images were observed using a transmission electron microscope (TEM, JEOL 2010) operating at 200 kV. The crystallinity was examined using X-ray diffractometer (Shimadzu) with Cu Kα irradiation. Fourier transform infrared spectroscopy (FTIR) (PerkinElmer) was utilized to identify the types of bonding in the samples. Probe X-ray photoelectron spectroscopy (XPS, ESCALab 250iXL and Thetaprobe A1333) was used to verify the valence state of iron and oxygen. Nitrogen adsorption/desorption isotherms were measured on a Micromeritics Tristar 3000 porosimeter (mesoporous characterization) and Micromeritics ASAP 2020 (microporous characterization) at 77 K. Samples were degassed at 100 °C for 6 h under vacuum before measurement. The specific surface areas were calculated using the Brunauer–Emmet–Teller (BET) method.

Battery Assembly and Electrochemical Characterization. 70 wt % active materials, 20 wt % single-wall CNT (SWCNT), and 10 wt % polyacrylonitrile (PAN) were mixed into *N*-methyl-2-pyrrolidinone (NMP). The obtained slurry was cast onto a copper foil (diameter: 12 mm) and dried in vacuum at 50 °C for 12 h to remove excess solvent. Electrochemical measurements were carried out on coin-type cells with lithium metal as both counter and reference electrode, Celgard 2400 membrane as the separator, and the electrolyte solution obtained by dissolving 1 M $LiPF_6$ into a mixture of ethylene carbonate (EC) and dimethyl carbonate (DMC) (EC/DMC, 50:50 w/w). The cells were tested on a NEWARE multichannel battery test system with galvanostatic charge and discharge (voltage window of 0.05–3.0 V). The electrochemical impedance measurement is performed at the OCV at all states of discharge and charge, with amplitude of 5 mV and in the frequency range of 10^5–0.01 Hz.

RESULTS AND DISCUSSION

Morphology Characterization. The amorphous nature of the synthesized product is revealed by the X-ray diffraction (XRD) pattern (Figure S1), which shows a broad hump in the 2θ range of 20°–35° without any characteristic peaks. In order to know the chemical composition and ensure the completeness of the oxidation process, X-ray photoelectron spectroscopy (XPS) was conducted to find out the oxidation state of Fe and O. The XPS scan profile (Figure S2) of the full range (0–1300 eV) reveals the presence of mainly Fe, O, and C, indicating complete reaction of iron sulfide and formation of iron oxides or iron oxyhydroxide. The $2p_{1/2}$ and $2p_{3/2}$ photoelectrons at 711 and 724 eV of the Fe 2p XPS data (Figure S3a) correspond to the reported values for Fe^{3+} in iron oxides or iron oxyhydroxide,[10] which confirms complete oxidation of Fe^{2+} to Fe^{3+}. The XPS spectrum of oxygen (Figure S3b) can be convoluted to three distinct peaks, indicating presence of oxygen in three different states. The two convoluted peaks at 530.10 and 531.50 eV can be assigned to O^{2-} and OH^- in FeOOH, respectively.[10] The other peak at 533.4 eV may be attributed to the oxygen in surface-absorbed water.[10b] To characterize the chemical bonds in this amorphous compound, Fourier transform infrared spectroscopy (FTIR) was conducted the wavenumber range of 400–4000 cm^{-1}. Figure S4 displays the FTIR spectrum of the amorphous sample and compares with its crystalline counterparts obtained by annealing the amorphous sample at 800 °C. The annealed sample is identified as α-Fe_2O_3 by XRD pattern in Figure S5. For both samples, broad adsorption bands at 3400 and 1640 cm^{-1} can be ascribed to the stretching vibration of O–H and vibrations of adsorbed water molecules, respectively.[11] The crystalline α-Fe_2O_3 shows evident adsorption bands at 465 and 549 cm^{-1}, which can be attributed to the bending and stretching of Fe–O bond, respectively.[12] However, the amorphous iron oxide shows only broad and weak adsorption bands in the characteristic adsorption range of Fe–O bond. The absorption peaks at 471 and 686 cm^{-1} can be assigned to the Fe–O vibrational modes in FeOOH. The Fe–O stretching vibration is responsible for the adsorption at around 618 cm^{-1} in FeOOH.[10b,11] Based on the results above, the synthesized product is identified to be amorphous iron (Fe^{3+}) oxyhydroxide (AIO).

The SEM image (Figure 1a) and low-magnification TEM image (Figure 1b) of the amorphous product reveal loose and

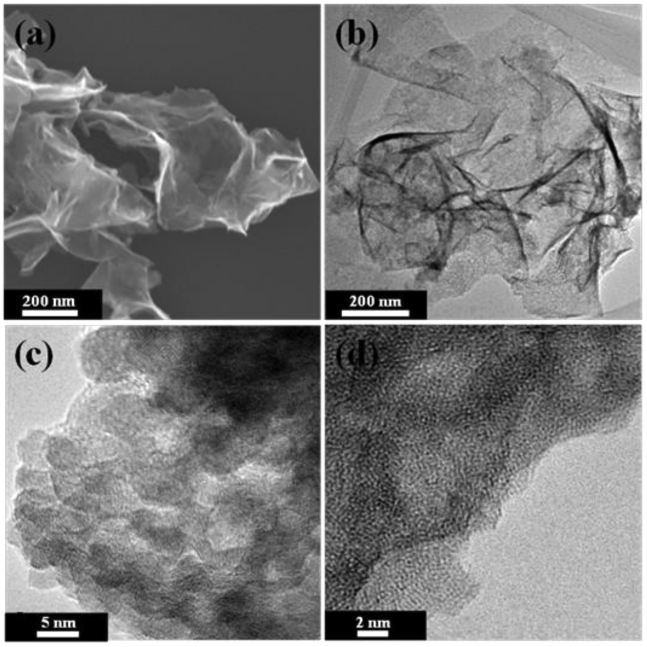

Figure 1. (a) SEM image. (b) TEM image. (c, d) HRTEM images of the amorphous iron oxyhydroxide nanosheet.

corrugated graphene-like 2D nanosheet structure, indicating no morphology and dimension change from its predecessor, iron sulfide nanosheets.[10b] The sulfide-to-oxide conversion process was conducted in deionized water with the assistance of cetrimonium bromide (CTAB) surfactant. The iron sulfide nanosheets were synthesized in organic solvent (oleylamine) and capped by organic surfactant. CTAB facilitates uniform dispersion of FeS nanosheets in water and prevents their agglomeration during oxidation (Figure S6). Observed from the HRTEM image (Figure 1c), individual nanosheet consists of

dx.doi.org/10.1021/jp405848j | J. Phys. Chem. C XXXX, XXX, XXX–XXX

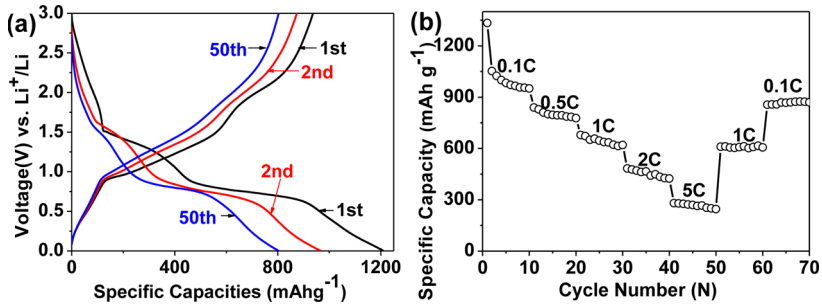

Figure 2. (a) Charge−discharge voltage profiles of the 1st, 2nd, and 50th cycle at a current density of 0.11 C (100 mA/g). (b) Cycling performance at different C rates.

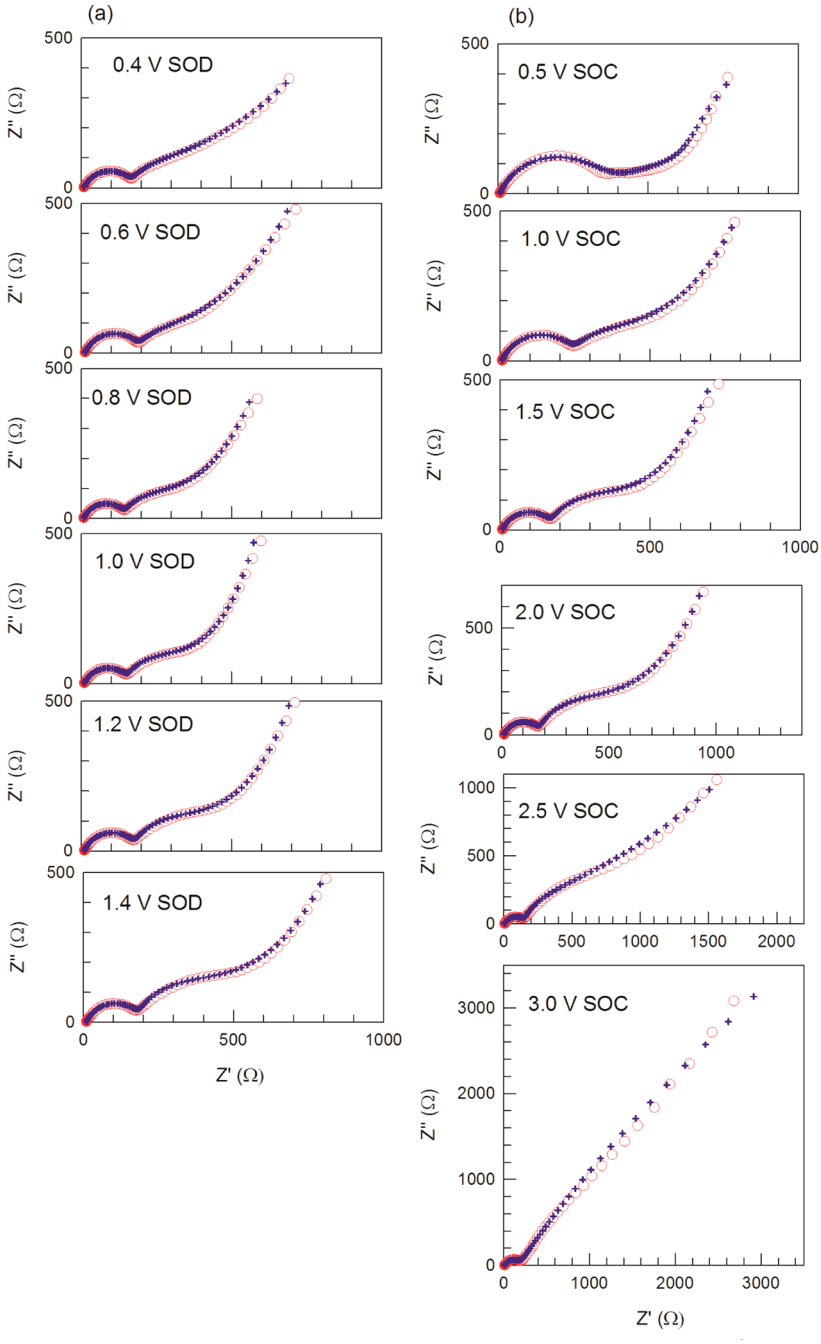

Figure 3. Impedance response measured at different voltages (vs Li^+/Li) corresponding either to (a) discharge regime SOD or (b) charge regime SOC. Experimental data (dot) and fits (cross) are displayed for comparison.

dx.doi.org/10.1021/jp405848j | J. Phys. Chem. C XXXX, XXX, XXX−XXX

nanoparticles aggregated in porous form. The diameters of the fine nanoparticles are less than 5 nm. As depicted by the HRTEM image (Figure 1d), the atomic lattice on the surface of nanosheets lacks regular periodicity, which further confirms the amorphous nature of the synthesized product. Nitrogen absorption/desorption measurements on the porous product determined a Brunauer–Emmett–Teller (BET) surface area of 233 $m^2\ g^{-1}$ (Figure S7). The adsorption hysteresis does not show any limiting adsorption at high p/p° (>0.7), which also implies the presence of slit-shaped pores given by the aggregates of loosely coherent very fine nanoparticles.[13] The highly porous nanostructure and high surface area are attractive for electrochemical applications.

Electrochemical Characterization. Figure 2a shows the voltage profile of the AIO nanosheet electrode at a current density of 100 mA g^{-1} between 0.05 and 3.0 V (vs Li^+/Li) for the 1st, 2nd, and 50th discharge/charge cycles. In the first cycle discharge, the Li insertion involves three distinguishable stages: a shallow slope between 2.8 and 1.5 V and two distinguishable plateaus at around 1.4 and 0.75 V, respectively. The specific discharge capacity amounts to 437 mAh g^{-1} when the AIO electrode is discharged to 0.95 V, which corresponds to incorporation of approximately 1.45 mol Li per mol of AIO (Figure S9). Ex-situ examination of the active material was carried out. TEM and HRTEM images of the active material discharged to 0.95 V (Figure S8a,b) demonstrate retention of its nanosheet morphology and amorphous nature. It is assumed that the initial two stages only involves surface Li storage and insertion of Li into the porous amorphous nanostructure.[14] The specific capacity of 914 mAh g^{-1} corresponds to the insertion of approximately insertion of 3 mol Li per mol of AIO at the discharge potential of 0.5 V, implying complete conversion reaction between Li and AIO with the formation of elemental Fe and Li_2O ($FeOOH + 3Li^+ + 3\ e^- \rightarrow Fe + Li_2O + LiOH$).[11,14] Based on this conversion reaction, the theoretical discharge capacity of iron oxyhydroxide is 903 mAh g^{-1}. The ex-situ TEM image (Figure S8c) of the active material at this discharged state shows that the structural network remains but the nanosheet has been partially destroyed. High-magnification TEM observation (Figure S8d) reveals formation of very fine nanorods. The first cycle discharge shows a total specific capacity of 1210 mAh g^{-1}, and the extra capacity can be attributed to surface solid–electrolyte interphase (SEI) layer formation.[15] The cycling performance of the AIO-based electrode at varying current densities is plotted in Figure 2b. It depicts fifth cycle discharge capacities of 985, 797, 642, 465, and 270 mAh g^{-1} at current densities of 0.1, 0.5, 1, 2, and 5 C, respectively (1 C = 903 mA g^{-1}). When the current density is changed to 1 and 0.1 C after cycling at 5 C, the electrode capacity is reduced to 607 and 870 mAh g^{-1}, respectively. The high porosity and large active surface area contribute to the high capacity of the AIO electrode but also cause continuous surface side reactions, which results in capacity fading upon cycling.[16] The AIO electrode demonstrates higher capacities than crystalline iron oxyhydroxide at the same current densities.[11,14,17] Some of the research reports proposed that the improved rate capability of amorphous electrode material results from higher lithium ion mobility in its loose structure and large quantities of structural defects.[6,18] However, for conversion-reaction type electrode materials, conversion-reaction kinetics plays a more determinative role in electrode rate capabilities than Li^+ diffusion does. Therefore, the conversion-reaction kinetics of the AIO electrode requires investigation.

EIS Analysis. Nyquist plots derived from impedance measurement and proposed equivalent circuits are usually combined in analyzing of electrode process kinetics in LIBs.[19] In recent research, EIS has been rigorously applied in explaining intercalation reactions to estimate charge transfer resistance and the diffusion coefficient of Li in intercalation-type electrode materials.[20] However, EIS has seldom been employed to study conversion reaction process. Nyquist plots of the EIS analysis of AIO nanosheet electrode at different states of discharge (SOD) and states of charge (SOC) during its fifth cycle are shown in Figures 3a and 3b, respectively. The fifth cycle is selected for analysis because the conversion reaction is expected to be reversible and stabilized afterward.

The Nyquist plots consist of three parts: the high-frequency semicircle (HFS), medium-frequency semicircle (MFS), and inclined low-frequency line (LFL). Some of the impedance features can be easily interpreted as originating from well-known processes. At high frequencies, a rather constant arc corresponds to the parallel connection between the double layer capacitance $C_{dl} \approx 45\ \mu F$ and surface charge transfer resistance $R_{ct} \approx 200\ \Omega$. An additional series resistance accounts for the solution contribution $R_s \approx 8\Omega$. The LFL signals the occurrence of a voltage-modulated process which gives rise to a capacitive behavior. The interpretation relies on the so-called chemical capacitance which informs on the electrode's ability of varying the concentration c of reacted Li^+ upon application of a differential change in the chemical potential μ (directly assimilated to the electrode potential upon steady-state conditions as $\mu = qV$, where q is the positive elementary charge).[21]

$$C_\mu^c = qL\frac{\partial c}{\partial V} \tag{1}$$

Here L represents the electrode thickness. The analysis of the MFS is much more speculative. As inferred by examining the impedance plots in Figure 3, the kinetics of the charging/discharging mechanism are dominated by the resistive contribution arising from MFS in comparison with R_{ct}. For intercalation compounds the rate-limiting mechanism is the diffusion of Li^+ inside the active material. In those materials the intermediate-frequency resistance arises from the transport of Li^+ before reaching stable sites within the matrix. Diffusion of ions gives rise to distinctive impedance patterns characterized by Warburg-like responses as $Z \propto (i\omega)^{-1/2}$ (being ω the angular frequency, and $i = (-1)^{1/2}$). In opposition to that impedance pattern, a well-defined arc is encountered at MFS for the electrodes studied here. Models based on spatially restricted ion diffusion were proposed to account for intermediate-frequency arcs relaying on a distribution of diffusion lengths,[22] or electronic transport limitations.[23] A commonly used approach stated the simultaneous occurrence of two-parallel diffusion paths of dissimilar lengths. However, the amorphous iron oxyhydroxide electrodes analyzed in this work function by conversion reactions that entail an overall material rearrangement in both chemical and structural nature. These considerations lead us to regard the conversion reaction as the rate-limiting process of the change in electrode state of charge/discharge. The corresponding resistive element is then labeled as conversion-reaction resistance R_{cr} and is connected in series with the previously introduced C_μ^c. A simple model accounting for the impedance of conversion reaction which

dx.doi.org/10.1021/jp405848j | J. Phys. Chem. C XXXX, XXX, XXX–XXX

explains the underlying meaning of the circuit elements is outlined in the next section. The model is able to capture the essential connection between C_μ^c and R_{cr} and the concentration and kinetics of reaction of ionic species. It is assumed that transport processes do not significantly contribute to the dissipative mechanism represented by the resistance. The circuit elements in series, R_{cr} and C_μ^c, allow us to calculate the conversion-reaction time scale as the product $R_{cr}C_\mu^c$. The reciprocal corresponds to the response frequency

$$\omega_{cr} = \frac{1}{R_{cr}C_\mu^c} \tag{2}$$

which establishes the reaction kinetic regime. The MFS appears as a consequence of the inclusion in parallel of an additional capacitive element of small value in comparison with C_μ^c (see below). Such capacitance is interpreted here as originated by the chemical capacitance corresponding to intercalated (not reacted) Li: C_μ^n (see below). An equivalent circuit model which gathers all the aforementioned mechanisms is shown in Figure 4. This equivalent circuit produces an excellent fit for the Nyquist plots in Figures 3a and 3b, both for charging and discharging polarization regimes.

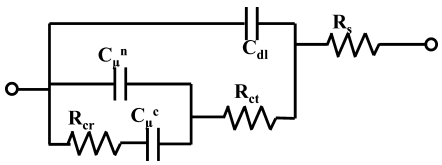

Figure 4. Equivalent circuit employed in fitting which includes double layer capacitance, electrolyte/electrode charge transfer resistance, and conversion reaction circuit elements.

Conversion-Reaction Equivalent Circuit. In the following a simple model accounting for the equivalent circuit of the conversion reaction mechanism will be derived. Let us express a conversion reaction as

$$Li^+ + MX + e^- \rightarrow M + LiX \tag{3}$$

where Li^+ is a lithium ion, M is a transition metal, and X = O, S, F.... The stoichiometry is neglected for simplicity. It has been widely recognized that the voltage dependence on charge for systems undergoing a conversion reaction can be divided in several parts.[24] In a first stage Li atoms enter the MX lattice in a usual intercalation process, with a marked step of the voltage. Thereafter, the reaction of eq 3 proceeds producing phase segregation. In order to obtain a physical interpretation for the results of impedance spectroscopy measurements, we outline here a simple model that incorporates the two above stages. This model is based on a well-known two-state model that has been often used for describing intercalation systems with different lattice sites and even including order−disorder transitions.[25] This model is rather crude for the present system; however, it is rather illustrative of the fact that measured capacitances are not of interfacial origin. Since the model obeys detailed balance, it incorporates time reversal properties, and the voltage hysteresis observed in conversion reactions cannot be described by this simple model.[26] It would be necessary to modify the kinetic coefficients in the model, which lies beyond the scope of the present work.

We assume that the MX lattice contains N_0 sites where Li^+ ions can diffuse and a total of N_1 atoms of type X per unit volume that form sites where Li^+ ions can react according to eq 3. $n \le N_0$ is the concentration of diffusing ions in the lattice with energy E_0 (we assume $n \ll N_0$), and $c \le N_1$ is the concentration of Li^+ that have reacted to LiX with energy E_1. The equilibrium chemical potential of Li^+ ions is

$$\mu = E_0 + k_B T \ln\left(\frac{n}{N_0}\right) = E_1 + k_B T \ln\left(\frac{c}{N_1 - c}\right) \tag{4}$$

Any change of voltage changes the concentration of Li^+ ions in the LiMX particle. The mobile Li^+ concentration at the surface relates to the voltage as

$$n = N_0 e^{-(E_0 - qV)/k_B T} \tag{5}$$

Li ions enter the particle, diffuse, and react. This process is described by the kinetic equations

$$\frac{\partial n}{\partial t} = -\frac{\partial J_n}{\partial x} - k_1 n(N_1 - c) + k_2 c(N_0 - n) \tag{6}$$

$$\frac{\partial c}{\partial t} = k_1 n(N_1 - c) - k_2 c(N_0 - n) \tag{7}$$

Here J_n is the flux at position x, and $k_{1,2}$ correspond to the kinetic constants. For simplicity, we consider a one-dimensional system of thickness L such that the injected current is $j = qJ_n(0)$ and $J_n(L) = 0$. We can also assume that diffusion in the lattice is quite fast with respect to the reaction kinetics. This means that n and c are homogeneous, so that we can integrate eq 6 with the result

$$\frac{\partial n}{\partial t} = \frac{J_n(0)}{L} - k_1 n(N_1 - c) + k_2 c(N_0 - n) \tag{8}$$

The impedance of diffusion in this model has been described in refs 25c and 27, but hereafter diffusion is ignored, as mentioned previously, assuming ion displacement is facile. In equilibrium the current is zero and we obtain

$$\frac{k_1}{k_2} = \frac{N_0 \bar{c}}{\bar{n}(N_1 - \bar{c})} \tag{9}$$

Since we assume that k_1 and k_2 are constant, the detailed balance condition is

$$\frac{k_1}{k_2} = e^{(E_0 - E_1)/k_B T} \tag{10}$$

In transient or voltage modulated conditions the concentration of n is modified by the external potential, and c will change toward the equilibrium value indicated in eq 4. For a modulation of the density $n = \bar{n} + \hat{n}$, we find by eq 5 that the free ion density modulation depends on voltage modulation as

$$\hat{n} = \frac{c_\mu^n}{q}\hat{V} \tag{11}$$

Here the quantity

$$c_\mu^n = q\frac{\partial n}{\partial V} = \frac{q^2 n}{k_B T} \tag{12}$$

is a chemical capacitance (per unit volume) of the freely moving ions intercalated in the lattice. Similarly, we define a chemical capacitance for the lithium ions in LiX sites (related to that previously introduced in eq 1)

dx.doi.org/10.1021/jp405848j | J. Phys. Chem. C XXXX, XXX, XXX−XXX

$$c_\mu^c = q\frac{\partial c}{\partial V} = \frac{q^2 c(N_1 - c)}{N_1 k_B T} \tag{13}$$

It should be observed that the chemical capacitance is correlated to the derivative of the voltage−composition curves. This capacitance is not related to positive−negative charge separation at an interface.[21] In the simple model outlined here c_μ is given by the entropy of ions in equivalent cites. In general, c_μ relates to the dependence of the chemical potential on the concentration and depends on any chemical force over the ions in the solid phase.

Modulation of the voltage with angular frequency ω changes the free ion density which produces a change of the reacted density as $c(t) = \bar{c} + \hat{c}$. By a Laplace transform and expanding to first order, we obtain from eq 7 the relationship

$$\hat{c} = \frac{k_1(N_1 - \bar{c})}{\omega_{cr} + i\omega}\hat{n} \tag{14}$$

where

$$\omega_{cr} = k_1\bar{n} + k_2 N_0 \tag{15}$$

is the characteristic kinetic frequency of the conversion reaction previously introduced in eq 2. On the other hand, eq 8 gives

$$[i\omega + k_1(N_1 - c)]\hat{n} = (k_1\bar{n} - k_2 N_0)\hat{c} + \frac{\hat{J}_n}{L} \tag{16}$$

Inserting eqs 11 and 12 in eq 16, we arrive at the result

$$\left(C_\mu^n i\omega + \frac{C_\mu^c i\omega}{1 + i\omega/\omega_{cr}}\right)\hat{V} = \hat{j} \tag{17}$$

Here $C_\mu^n = Lc_\mu^n$ and $C_\mu^c = Lc_\mu^c$ are chemical capacitances per unit area. The admittance is defined as $Y = \hat{j}/\hat{V}$; therefore, we have

$$Y = C_\mu^n i\omega + {Z_{cr}}^{-1} \tag{18}$$

where

$$Z_{cr} = R_{cr} + \frac{1}{C_\mu^c i\omega} \tag{19}$$

Here we have introduced the resistance of the conversion reaction R_{cr} given by

$$\begin{aligned} {R_{cr}}^{-1} &= C_\mu^c \omega_{cr} \\ &= \frac{Lq^2}{N_1 k_B T}\bar{c}(N_1 - \bar{c})(k_1\bar{n} + k_2 N_0) \end{aligned} \tag{20}$$

The impedance model in eq 18 corresponds to the previously introduced equivalent circuit in Figure 4.

Although the conversion reaction involves insertion and release of charges, we propose here that the rate-limiting process is the reaction itself but not the ion transport. It can be modeled by means of a discharge and charge process as a series *RC* circuit. As explained previously, the time required for complete change in SOD/SOC of a series *RC* circuit is given by the product $R_{cr}C_\mu^c$. The larger the time constant, the longer time is required for discharging or charging to the target voltage. The electrical parameters at different SOD and SOC have also been calculated from fitting and displayed in Figure 5. It is observed that C_μ^c exhibits a high value of order 0.1 F. For voltages in excess of 0.6 V, C_μ^c shows slight variations between 0.05 and 0.10 F and exhibits a small peak at ∼0.7 V, in good correlation

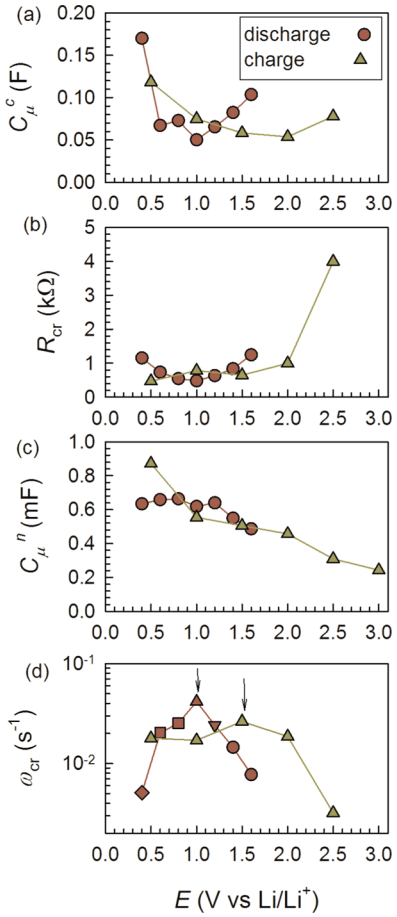

Figure 5. Parameters at different SOD and SOC extracted from fitting using the equivalent circuit in Figure 4. Lines used to guide the eyes. (a) Chemical capacitance corresponding to concentration of reacted Li^+. (b) Conversion-reaction resistance. (c) Chemical capacitance corresponding to moving Li^+. (d) Conversion-reaction response frequency. Arrows signal the shift in the maximum frequency related to the voltage hysteresis.

with the plateau of the discharge voltage profile in Figure 2a. The conversion reaction resistance R_{cr} demonstrates similar trends (Figure 5b) but exhibits much larger values for high voltages (>2 V). This entails that the conversion reaction is hindered at high states of charge but is favored when the ion concentration is high within the electrode. An averaged value $R_{cr} \approx 500\ \Omega$ is encountered greater than R_{ct}. It is evidenced that the intermediate capacitance C_μ^n related to intercalated Li^+ concentration (Figure 5c) shows values 2 orders of magnitude below C_μ^c, which accounts for concentration of reacted species The combination of C_μ^c, R_{cr}, and C_μ^n forms a sort of relaxation subcircuit[28] which is interpreted here in terms of the conversion-reaction mechanism.

The conversion-reaction kinetics can be alternatively accessed by examining the response frequency in eq 2. Values of ω_{cr} below 0.04 s^{-1} are found. One can observe that ω_{cr} exhibits a maximum (marked with an arrow in Figure 5d), which is located within the potential interval of the major conversion reaction ($FeOOH + 3Li^+ + 3e^- \rightarrow Fe + Li_2O + LiOH$) according to the discharge voltage profile (Figure 2a). We notice that a voltage shift in ω_{cr} of ∼0.5 V occurs between discharge and charge regimes. This fact points to the hysteretic behavior of the conversion reaction.[29] We highlight that EIS analysis reproduces the hysteresis observed between charge and

dx.doi.org/10.1021/jp405848j | J. Phys. Chem. C XXXX, XXX, XXX−XXX

discharge profiles (Figure 2a) or cyclic voltammetry. It can be inferred accordingly that the conversion-reaction hysteresis has an origin related to the intrinsic thermodynamics rather than to transport limitations.

CONCLUSIONS

In summary, amorphous iron oxyhydroxide nanosheet has been synthesized via surfactant-assisted oxidation of the iron sulfide nanosheet. The highly porous nanostructure and high surface area of the amorphous iron oxyhydroxide nanosheet are attractive for electrochemical applications. When characterized as anode material in LIB, it has conversion reaction with Li^+ and demonstrates superior rate capability (e.g., discharge capacity as high as 465 mAh g^{-1} is delivered at a current density of 2 C). A new equivalent circuit that directly models the conversion reaction process was set up by fitting the Nyquist plots from EIS analysis. The conversion-reaction subcircuit (series *RC*) reproduces the hysteresis in the discharge/charge voltage profile, indicating that the hysteresis behavior has a thermodynamic origin rather than being limited by Li transport.

ASSOCIATED CONTENT

Supporting Information

XRD pattern, XPS spectrum, FTIR spectrum, BET isotherm profile of as-synthesized amorphous iron oxyhydroxide, and scheme of the oxidation reaction and post-mortem analysis of cycled electrode materials. This material is available free of charge via the Internet at http://pubs.acs.org.

AUTHOR INFORMATION

Corresponding Author

*E-mail: alexyan@ntu.edu.sg (Q.Y.); garciag@fca.uji.es (G.G.-B.).

Notes

The authors declare no competing financial interest.

ACKNOWLEDGMENTS

We thank financial support from Generalitat Valenciana (ISIC/2012/008 Institute of Nanotechnologies for Clean Energies) and FP7 European project ORION (Large CP-IP 229036-2). We thank the financial support by the Singapore National Research Foundation (NRF) through its Campus for Research Excellence and Technological Enterprise (CREATE) program.

REFERENCES

(1) Tarascon, J. M.; Armand, M. Issues and challenges facing rechargeable lithium batteries. *Nature* **2001**, *414* (6861), 359−367.

(2) (a) Zhu, J.; Sun, K.; Sim, D.; Xu, C.; Zhang, H.; Hng, H. H.; Yan, Q. Nanohybridization of ferrocene clusters and reduced graphene oxides with enhanced lithium storage capability. *Chem. Commun.* **2011**, *47* (37), 10383−10385. (b) Wang, Z.; Luan, D.; Madhavi, S.; Li, C. M.; Lou, X. W. α-Fe_2O_3 nanotubes with superior lithium storage capability. *Chem. Commun.* **2011**, *47* (28), 8061−8063. (c) Wang, B.; Chen, J. S.; Wu, H. B.; Wang, Z.; Lou, X. W. Quasiemulsion-templated formation of α-Fe_2O_3 hollow spheres with enhanced lithium storage properties. *J. Am. Chem. Soc.* **2011**, *133* (43), 17146−17148.

(3) France Patent 1490725, 1966.

(4) Guan, D.; Cai, C.; Wang, Y. Amorphous and crystalline TiO_2 nanotube arrays for enhanced li-ion intercalation properties. *J. Nanosci. Nanotechnol.* **2011**, *11* (4), 3641−3650.

(5) Wang, X.-L.; Han, W.-Q.; Chen, H.; Bai, J.; Tyson, T. A.; Yu, X.-Q.; Wang, X.-J.; Yang, X.-Q. Amorphous hierarchical porous GeO_x as high-capacity anodes for li ion batteries with very long cycling life. *J. Am. Chem. Soc.* **2011**, *133* (51), 20692−20695.

(6) Ku, J. H.; Ryu, J. H.; Kim, S. H.; Han, O. H.; Oh, S. M. Reversible lithium storage with high mobility at structural Defects in amorphous molybdenum dioxide electrode. *Adv. Funct. Mater.* **2012**, *22*, 3658−3664.

(7) (a) Controlled synthesis and gas-sensing properties of hollow sea urchin-like α-Fe_2O_3 nanostructures and α-Fe_2O_3 nanocubes. *Sens. Actuators, B* **2009**, *141* (2), 381. (b) Flexible morphology-controlled synthesis of mesoporous hierarchical α-Fe_2O_3 architectures and their gas-sensing properties. *CrystEngComm* **2011**, *13* (3), 806. (c) Synthesis of spindle-shaped α-FeOOH and α-Fe_2O_3 nanocrystals. *Cryst. Res. Technol.* **2011**, n/a. (d) Tabuchi, T.; Katayama, Y.; Nukuda, T.; Ogumi, Z. Surface reaction of β-FeOOH film negative electrode for lithium-ion cells. *J. Power Sources* **2009**, *191* (2), 636−639.

(8) (a) Zhu, J.; Yin, Z.; Yang, D.; Sun, T.; Yu, H.; Hoster, H. E.; Hng, H. H.; Zhang, H.; Yan, Q. Hierarchical hollow spheres composed of ultrathin Fe_2O_3 nanosheets for lithium storage and photocatalytic water oxidation. *Energy Environ. Sci.* **2013**, *6* (3), 987−993. (b) Zhang, W.; Zeng, Y.; Xu, C.; Tan, H.; Liu, W.; Zhu, J.; Xiao, N.; Hng, H. H.; Ma, J.; Hoster, H. E.; Yazami, R.; Yan, Q. Fe_2O_3 nanocluster-decorated graphene as O_2 electrode for high energy Li-O_2 batteries. *RSC Adv.* **2012**, *2* (22), 8508−8514. (c) Reddy, M. V.; Yu, T.; Sow, C. H.; Shen, Z. X.; Lim, C. T.; Subba Rao, G. V.; Chowdari, B. V. R. α-Fe_2O_3 nanoflakes as an anode material for Li-ion batteries. *Adv. Funct. Mater.* **2007**, *17* (15), 2792−2799.

(9) Xu, C.; Zeng, Y.; Rui, X.; Xiao, N.; Zhu, J.; Zhang, W.; Chen, J.; Liu, W.; Tan, H.; Hng, H. H.; Yan, Q. Controlled soft-template synthesis of ultrathin C@FeS nanosheets with high-Li-storage performance. *ACS Nano* **2012**, *6* (6), 4713−4721.

(10) (a) Sun, Z.; Feng, X.; Hou, W. Morphology-controlled synthesis of α-FeOOH and its derivatives. *Nanotechnology* **2007**, *18* (45), 455607. (b) Mansour, A. N.; Brizzolara, R. A. Characterization of the surface of α-FeOOH powder by XPS. *Surf. Sci. Spectra* **1996**, *4* (4), 357−362.

(11) Zhang, C.; Zhu, J.; Rui, X.; Chen, J.; Sim, D.; Shi, W.; Hng, H. H.; Lim, T. M.; Yan, Q. Synthesis of hexagonal-symmetry α-iron oxyhydroxide crystals using reduced graphene oxide as a surfactant and their Li storage properties. *CrystEngComm* **2012**, *14* (1), 147−153.

(12) Wang, Y.; Muramatsu, A.; Sugimoto, T. FTIR analysis of well-defined α-Fe_2O_3 particles. *Colloids Surf., A* **1998**, *134* (3), 281−297.

(13) Sing, K. S. W.; Everett, D. H.; Haul, R. A. W.; Moscou, L.; Pierotti, R. A.; Rouquerol, J.; Siemieniewska, T. Reporting physisorption data for gas/solid systems with special reference to the determination of surface area and porosity. *Pure Appl. Chem.* **1985**, *57* (4), 603−619.

(14) Lou, X.; Wu, X.; Zhang, Y. Goethite nanorods as anode electrode materials for rechargeable Li-ion batteries. *Electrochem. Commun.* **2009**, *11* (8), 1696−1699.

(15) Pinson, M. B.; Bazant, M. Z. Theory of SEI Formation in rechargeable batteries: capacity fade, accelerated aging and lifetime prediction. *J. Electrochem. Soc.* **2012**, *160* (2), A243−A250.

(16) (a) Arora, P.; White, R. E.; Doyle, M. Capacity fade mechanisms and side reactions in lithium−ion batteries. *J. Electrochem. Soc.* **1998**, *145* (10), 3647−3667. (b) Sikha, G.; Popov, B. N.; White, R. E. Effect of porosity on the capacity fade of a lithium-ion battery: theory. *J. Electrochem. Soc.* **2004**, *151* (7), A1104−A1114.

(17) Li, X.; Meng, X.; Liu, J.; Geng, D.; Zhang, Y.; Banis, M. N.; Li, Y.; Yang, J.; Li, R.; Sun, X.; Cai, M.; Verbrugge, M. W. Batteries: tin oxide with controlled morphology and crystallinity by atomic layer deposition onto graphene nanosheets for enhanced lithium storage. *Adv. Funct. Mater.* **2012**, *22* (8), 1646−1646.

(18) Wang, Z.; Wang, Z.; Liu, W.; Xiao, W.; Lou, X. W. Amorphous $CoSnO_3$@C nanoboxes with superior lithium storage capability. *Energy Environ. Sci.* **2013**, *6* (1), 87−91.

(19) Xiang, J. Y.; Tu, J. P.; Qiao, Y. Q.; Wang, X. L.; Zhong, J.; Zhang, D.; Gu, C. D. Electrochemical impedance analysis of a hierarchical CuO electrode composed of self-assembled nanoplates. *J. Phys. Chem. C* **2011**, *115* (5), 2505−2513.

(20) (a) Wang, C.; Appleby, A. J.; Little, F. E. Electrochemical impedance study of initial lithium ion intercalation into graphite powders. *Electrochim. Acta* **2001**, *46* (12), 1793−1813. (b) Wang, C.; Hong, J. Ionic/electronic conducting characteristics of $LiFePO_4$ cathode materials: the determining factors for high rate performance. *Electrochem. Solid-State Lett.* **2007**, *10* (3), A65−A69.
(21) Bisquert, J. Chemical capacitance of nanostructured semiconductors: its origin and significance for heterogeneous solar cells. *Phys. Chem. Chem. Phys.* **2003**, *5*, 5360−5364.
(22) Levi, M. D.; Aurbach, D. Impedance of a single intercalation particle and of non-homogeneous, multilayered porous composite electrodes for Li-ion batteries. *J. Phys. Chem. B* **2004**, *108*, 11693−11703.
(23) Meyers, J. P.; Doyle, M.; Darling, R. M.; Newman, J. The impedance response of a porous electrode composed of intercalation particles. *J. Electrochem. Soc.* **2000**, *147* (8), 2930−2940.
(24) (a) Ponrouch, A.; Palacín, M. R. Optimisation of performance through electrode formulation in conversion materials for lithium ion batteries: Co_3O_4 as a case example. *J. Power Sources* **2012**, *212* (0), 233−246. (b) Khatib, R.; Dalverny, A.-L.; Saubanère, M.; Gaberscek, M.; Doublet, M.-L. Origin of the voltage hysteresis in the CoP conversion material for Li-ion batteries. *J. Phys. Chem. C* **2013**, *117*, 837−849.
(25) (a) McKinnon, W. R.; Haering, R. R. Physical mechanisms of intercalation. In *Modern Aspects of Electrochemistry*; White, R. E., Bockris, J. O. M., Conway, B. E., Eds.; Plenum Press: New York, 1983; Vol. *15*, pp 235−304. (b) Gao, Y.; Reimers, J. N.; Dahn, J. R. Changes in the voltage profile of $Li/Li_{1+x}Mn_{2-x}O_4$ cells as a function of x. *Phys. Rev. B* **1996**, *54*, 3878−3883. (c) Bisquert, J.; Vikhrenko, V. S. Analysis of the kinetics of ion intercalation. Two state model describing the cpupling of solid state ion diffusion and ion binding processes. *Electrochim. Acta* **2002**, *47*, 3977−3988.
(26) Khatib, R.; Dalverny, A.-L.; Saubanère, M.; Gaberscek, M.; Doublet, M.-L. Origin of the voltage hysteresis in the CoP conversion material for Li-ion batteries. *J. Phys. Chem. C* **2013**, *117*, 837−849.
(27) (a) Levi, M. D.; Gizbar, H.; Lancry, E.; Gofer, Y.; Levi, E.; Aurbach, D. A comparative study of Mg^{2+} and Li^+ ion insertions into the Mo_6S_8 Chevrel phase using electrochemical impedance spectroscopy. *J. Electroanal. Chem.* **2004**, *569*, 211−223. (b) Levi, M. D.; Aurbach, D. Distinction between energetic inhomogeneity and geometric non-uniformity of ion insertion electrodes based on complex impedance and complex capacitance analysis. *J. Phys. Chem. B* **2005**, *109*, 2763−2773.
(28) Garcia-Belmonte, G.; Bueno, P. R.; Fabregat-Santiago, F.; Bisquert, J. Relaxation processes in the coloration of amorphous WO_3 thin films studied by combined impedance and electro-optical measurements. *J. Appl. Phys.* **2004**, *96*, 853−859.
(29) (a) Cabana, J.; Monconduit, L.; Larcher, D.; Palacín, M. R. Beyond intercalation-based Li-ion batteries: The state of the art and challenges of electrode materials reacting through conversion reactions. *Adv. Mater.* **2010**, *22* (35), E170−E192. (b) Khatib, R.; Dalverny, A. L.; Saubanère, M.; Gaberscek, M.; Doublet, M. L. Origin of the voltage hysteresis in the CoP conversion material for Li-ion batteries. *J. Phys. Chem. C* **2012**, *117* (2), 837−849.

■ NOTE ADDED AFTER ASAP PUBLICATION

This paper was published on the Web on August 1, 2013, with errors to Figures 3 and 5 and reference 17. The corrected version was reposted on August 16, 2013.